nuclear fusion
IAEA

PAPER • OPEN ACCESS

Impurity transport in ion- and electron-root confinement scenarios at Wendelstein 7-X

To cite this article: A. Langenberg *et al* 2021 *Nucl. Fusion* **61** 116018

View the article online for updates and enhancements.

You may also like

- Investigation of turbulence rotation in limiter plasmas at W7-X with newly installed poloidal correlation reflectometer
A. Krämer-Flecken, T. Windisch, W. Behr et al.

- Major results from the first plasma campaign of the Wendelstein 7-X stellarator
R.C. Wolf, A. Ali, A. Alonso et al.

- Energy confinement of hydrogen and deuterium electron-root plasmas in the Large Helical Device
Felix Warmer, H. Takahashi, K. Tanaka et al.

IOP ebooks™

Bringing together innovative digital publishing with leading authors from the global scientific community.

Start exploring the collection–download the first chapter of every title for free.

This content was downloaded from IP address 129.13.72.195 on 30/11/2021 at 10:01

OPEN ACCESS
IOP Publishing | International Atomic Energy Agency Nuclear Fusion
Nucl. Fusion **61** (2021) 116018 (6pp) https://doi.org/10.1088/1741-4326/ac24d4

Impurity transport in ion- and electron-root confinement scenarios at Wendelstein 7-X

A. Langenberg[1,*], Th. Wegner[1], O. Marchuk[2], J.M. García-Regaña[3], N.A. Pablant[4], G. Fuchert[1], S. Bozhenkov[1], H. Damm[1], E. Pasch[1], K.-J. Brunner[1], J. Knauer[1], M. Beurskens[1], F. Reimold[1], R.C. Wolf[1] and the W7-X Team[a]

[1] Max-Planck-Institut für Plasmaphysik, 17491 Greifswald, Germany
[2] Forschungszentrum Jülich GmbH, Institut für Energie- und Klimaforschung, 52425 Jülich, Germany
[3] Laboratorio Nacional de Fusión, CIEMAT, Av. Complutense, 28040, Spain
[4] Princeton Plasma Physics Laboratory, Princeton, NJ 08543, United States of America

E-mail: andreas.langenberg@ipp.mpg.de

Received 30 May 2021, revised 11 August 2021
Accepted for publication 8 September 2021
Published 29 September 2021

Abstract

This paper reports on the observation of enhanced Ar impurity confinement in high density, turbulence reduced ion-root confinement (IRC) scenarios in Wendelstein 7-X (W7-X). Compared to the central electron-root confinement (CERC), Ar densities are substantially increased up to one order of magnitude and Ar flux profiles switch from slightly positive to pronounced negative fluxes all along the plasma radius in IRC. Estimations of the diffusive D and convective V transport parameter profiles using the STRAHL impurity transport code suggest a fundamentally different behavior in CERC and IRC with, compared to neoclassical values, high diffusive D and typical V profiles in CERC versus strongly reduced D and pronounced negative V profiles in IRC.

Keywords: impurity transport, confinement, central electron-root confinement, microturbulence, ion root

(Some figures may appear in colour only in the online journal)

1. Introduction

The transport of impurities in the magnetic confined fusion device W7-X of the stellarator type is expected to be fundamentally different as compared to tokamaks. Due to its three dimensional magnetic field structure, stellarator specific impurity transport effects like the built-up of a radial electric field [1–3], variations of the electrostatic potential [4–6], or specific characteristics in the mixed collisionality regime [7–10] are theoretically expected. Some of these effects are expected to lead to increased confinement of impurities which can potentially cause a degradation of plasma performance or undesired radiative collapses of the plasma [11, 12]. Therefore, starting from the beginning of W7-X operations, the monitoring of impurity concentrations has been routinely performed using various complementary diagnostics [13–18]. Although predicted by neoclassical theory for specific plasma conditions, no impurity accumulation in medium density plasmas in the core electron root confinement (CERC) regime [19] has been observed in W7-X: short impurity confinement times, on the order of the energy confinement time, and a lack of impurity accumulation has been observed over a wide range of different impurity species and plasma conditions including long pulse operation of up to 120 s [20, 21]. As currently discussed, the reason for this absence of impurity accumulation can be attributed to a combination of a strong anomalous transport contribution [20, 22], most likely caused by microturbulence

* Author to whom any correspondence should be addressed.
[a] See Klinger *et al* 2019 (https://doi.org/10.1088/1741-4326/ab03a7) for the W7-X Team.

Original content from this work may be used under the terms of the Creative Commons Attribution 4.0 licence. Any further distribution of this work must maintain attribution to the author(s) and the title of the work, journal citation and DOI.

[10, 20, 23–25], and the presence of a positive neoclassical radial electric field (electron root) in a large portion of the plasma radius. However, with increasing density and, consequently, better collisional coupling between species, the thermalization among ions and electrons yields the plasma to be in ion root conditions (IRC) across the plasma core [26]. In the particular case of the injection of cryogenic hydrogen pellets, one additionally observes a significantly increased energy confinement and reduced anomalous transport in the IRC [27–29]. As in past experiments, energy confinement and impurity confinement have shown to be strongly coupled [21, 30], one would also expect an enhanced impurity confinement in IRC plasmas compared to CERC plasma scenarios.

In this work, a direct comparison of experimentally obtained Ar impurity transport is shown for a dedicated experiment program with a CERC to IRC and back to CERC transition [26], including pellet injections in the IRC phase. Making use of x-ray imaging spectrometer data, the temporal evolution of Ar^{15+}, Ar^{16+}, and Ar^{17+} density profiles are inferred using Bayesian analysis [14, 31] and from those, the Ar^{16+} flux Γ_{Ar16+} is derived using a previously developed neighboring charge state method [32].

After an introduction of the experimental method in section 2, the temporal evolution of experimentally observed Ar density and flux profiles is shown in section 3 comparing CERC and IRC scenarios. Finally, section 4 compares STRAHL simulated Ar density profiles to experimental ones for given D and V profiles, assuming reduced diffusion and negative, inwards directed convection of impurities in the IRC scenario.

2. Experimental method

For the characterization of Ar impurity transport at W7-X, the dynamic evolution of Ar densities and Ar fluxes has been evaluated during two different confinement scenarios CERC and IRC, both of which are seen within one experiment program.

In this study, Ar is used as a trace impurity for diagnostic purposes using the x-ray imaging crystal spectrometer (XICS) installed at W7-X [33]. As a noble gas, Ar is seen to have a high recycling coefficient close to one and, given constant plasma conditions, will maintain a constant density over several seconds after initial injection. This behavior of Ar is beneficial for the analysis performed here, as the impurity transport can be studied over an extended time interval without the need of refilling impurities, as in the case of non-recycling species like Ca, Al, Fe or others [15, 20, 34–36]. In the experiment programs discussed below, a single gas puff 100 ms after the start of ECR heating induced a small, non perturbing amount of Ar with $n_{Ar}/n_e \approx 2 \times 10^{-5}$.

For spatial resolution along the radial coordinate up to the last closed flux surface, Ar impurity flux profiles $\Gamma_{Ar}(\rho)$ are determined from Ar density profiles $n_{Ar}(\rho)$ measured by XICS. With its viewing geometry covering a large cross section of the plasma from the center toward the plasma edge, line integrated, radially resolved spectra of highly charged Ar are observed, yielding (beside ion and electron temperature profiles $T_i(\rho)$ and $T_e(\rho)$ and radial electric field profiles $E_r(\rho)$ [26]) also $n_{Ar}^{15+}(\rho)$, $n_{Ar}^{16+}(\rho)$, and $n_{Ar}^{17+}(\rho)$ density profiles from a spectral fit and tomographic inversion of the XICS data [21]. Note that XICS is currently not absolutely calibrated and there is an unknown calibration factor to the Ar density, yielding however correct Ar density profile shapes as well as a precise relative scaling between n_{Ar}^{15+}, n_{Ar}^{16+}, and n_{Ar}^{17+} profiles. Throughout this paper, $\rho = \sqrt{\psi/\psi_L}$ is defined as the square root of the poloidal magnetic flux ψ, normalized by the magnetic flux of the last closed flux surface ψ_L and $r = a\sqrt{\psi/\psi_L}$ is the effective radius with the minor plasma radius $a = 0.51$ m for the standard W7-X magnetic configuration considered here. From the three neighboring Ar charge state profiles, the $\Gamma_{Ar}^{16+}(\rho)$ flux profile can be derived by integration of the continuum equation

$$\frac{\partial n_{Ar^{16+}}}{\partial t} = -\frac{1}{r}\frac{\partial}{\partial r}(r\,\Gamma_{Ar^{16+}}) + S \tag{1}$$

over the effective radius $r = a\rho$

$$\Gamma_{Ar^{16+}}(r) = -\frac{1}{r}\int_0^r \frac{\partial n_{Ar^{16+}}}{\partial t} r'\,\mathrm{d}r' + \frac{1}{r}\int_0^r S r'\,\mathrm{d}r' \tag{2}$$

with sinks and sources S of Ar^{16+} determined by recombination R and ionization I rate coefficients of Ar^{15+}, Ar^{16+}, and Ar^{17+}

$$S = n_e\left(I_{Ar^{15+}} n_{Ar^{15+}} - I_{Ar^{16+}} n_{Ar^{16+}} - R_{Ar^{16+}} n_{Ar^{16+}} + R_{Ar^{17+}} n_{Ar^{17+}}\right) \tag{3}$$

taken from the ADAS database [37]. Charge exchange recombination being important especially at the plasma edge was not included in the analysis. A detailed description of the method can be found in reference [32].

3. Measured Ar density and Ar flux profiles in CERC and IRC

In figures 1(*a*)–(*c*), time traces of the line of sight integrated electron density n_e derived from the interferometer diagnostic [38], the electron cyclotron resonance heating power P_{ECRH}, and the temporal evolution of Ar density $n_{Ar}^{16+}(\rho)$, and Ar flux $\Gamma_{Ar}^{16+}(\rho)$ profiles are shown for the experiment program 201 712 07.006. Within this program, a CERC to IRC and back to CERC transition takes place that is driven by the injection of cryogenic hydrogen pellets [26], with improved energy confinement and reduced turbulence levels in the post-pellet IRC phase observed for this particular program [27], induced by a central density peaking as a consequence of the injection of cryogenic hydrogen pellets [39]. In the CERC phase (figure 2(*i*)), the radial electric field E_r is positive in the core plasma ($E_r(\rho < 0.5) = 15$ kV m^{-1}) and negative in the edge plasma ($E_r(\rho > 0.5) = -10$ kV m^{-1}), while in the post-pellet IRC (figure 2(*k*)), E_r is negative along the entire plasma radius with minimum values of $E_r \approx -20$ kV m^{-1} [26].

In the time interval $t = 1.5$–2.5 s (see dashed vertical lines in figure 1), a pure IRC, that is a negative radial electric field along the entire plasma radius, is present. For $t < 1.25$ s and $t > 2.75$ s, the plasma is under CERC conditions and in between, there are two transition phases when the CERC E_r

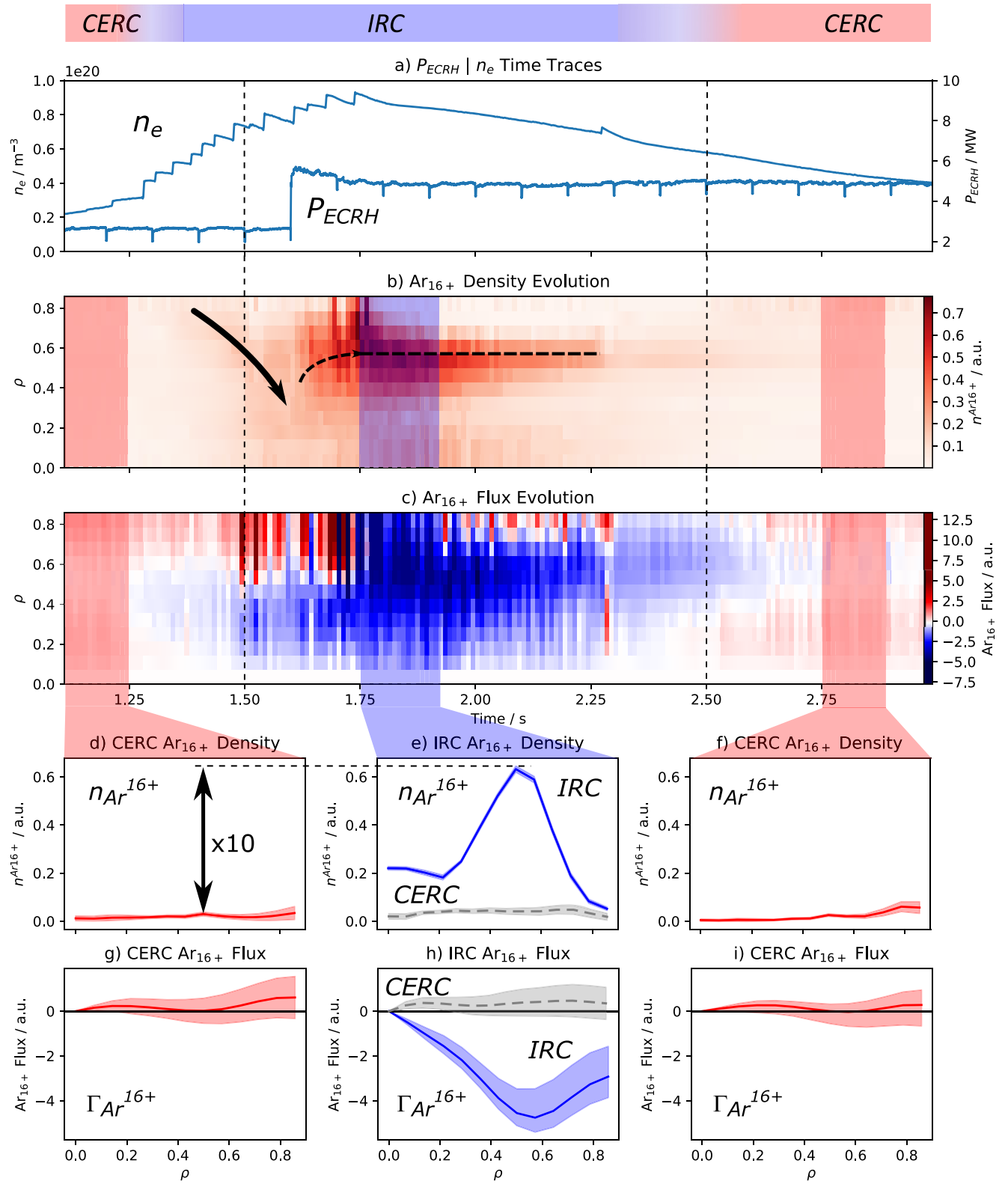

Figure 1. (*a*) Time traces of line integrated electron density and ECRH heating power. (*b*) Temporal evolution of Ar density profiles. (*c*) Temporal evolution of Ar flux profiles. (*d*)–(*f*) Ar density profiles for CERC (red) and IRC (blue) scenarios. (*g*)–(*i*) Ar flux profiles for CERC (red) and IRC (blue) scenarios.

slowly develops toward the IRC E_r for $t = 1.25$–1.5 s and back from IRC to CERC E_r for $t = 1.5$–2.75 s.

The above discussed dynamic evolution of E_r and change of the turbulent transport do have a significant impact on the Ar density and fluxes, as shown in figures 1(*b*) and (*c*): in both CERC phases, marked by the red shaded areas, the observed n_{Ar}^{16+} profiles are rather flat and the Γ_{Ar}^{16+} profiles are close to zero or slightly positive, see also figures 1(*d*), (*g*) and (*f*), (*i*).

In contrast, the IRC phase (blue shaded areas) shows highly peaked n_{Ar}^{16+} profiles at $\rho = 0.5$ with steep density gradients, both positive and negative, and absolute densities increased by a factor of 10 compared to the CERC scenario, see solid line in figure 1(*e*). Also the Ar flux profile changes from slightly positive to significant negative fluxes in the IRC with a maximum negative flux at $\rho = 0.5$, see solid line in figure 1(*h*). Apparently, the Ar flux profiles are strongly coupled to the evolution of the radial electric field and changes in the turbulent transport properties: in pure IRC with negative E_{r}, Ar fluxes are also significantly negative while in CERC, the Ar fluxes are close to zero or slightly positive. Moreover, in the E_{r} transition phases mentioned above, also the Ar fluxes steadily develop from the CERC to the IRC fluxes, very similar to the E_{r} profile evolutions [26].

The here observed n_{Ar}^{16+} profile evolution can be understood in terms of the $\Gamma_{\mathrm{Ar}}^{16+}$ fluxes: with the onset of the IRC and the development of negative Ar fluxes close to the plasma center at $\rho = 0.2$ for $t = 1.25$–1.6 s (figure 1(*c*)), the Ar density starts to rise and is attracted toward the plasma center as indicated by the solid arrow in figure 1(*b*). With the onset of the 5 MW heating power, the radial position of the Ar flux minimum is shifted radially outwards to $\rho = 0.6$, accompanied by a change of the peaking position of the n_{Ar}^{16+} profile also toward $\rho = 0.6$, see dashed horizontal line in figure 1(*b*) and an overall increase of the Ar^{16+} density and flux. With the gradually decreasing negative Ar flux for $t = 1.8$–2.5 s, also the Ar density decreases until the Ar flux is close to zero for $t > 2.6$ s and also the Ar densities become broad as before the onset of the IRC.

As the Ar^{16+} density profile is also determined by the T_{e} profile, and the central T_{e} drops from 5 keV to 2 keV during the CERC to IRC transition (see also figures 2(*a*) and (*b*)), it is not obvious to what extend the observed Ar^{16+} density peaking in IRC may also be caused by the T_{e} reduction. To explore this, the Ar^{16+} density and flux profiles of the experiment program 201 808 09.027 with a low central T_{e} value of 2 keV but in CERC conditions have been evaluated and shown in dashed lines in figures 1(*e*) and (*h*) for a direct comparison to the post-pellet IRC case. As can be seen, the $T_{\mathrm{e}} = 2$ keV CERC Ar density and flux (dashed lines in figures 1(*e*) and (*h*)) differ strongly from the $T_{\mathrm{e}} = 2$ keV IRC scenario, but are nearly identical to the $T_{\mathrm{e}} = 5$ keV CERC Ar density and flux profiles in figures 1(*d*), (*g*) and (*f*), (*i*), showing the T_{e} effect on the Ar profiles and fluxes being negligible compared to the effect of changing the confinement scenario from CERC to IRC.

The existence of two different confinement scenarios is further supported by the fact that impurity and energy confinement are increased, despite the heating power was stepped up from 3 to 5 MW. Following a simple scaling law however, one would expect a reduced confinement with increased heating power for both, energy [40] and impurity confinement [21].

4. Modeled Ar density and transport parameter profiles in CERC and IRC

For a better understanding of the observed changes in the transport properties of CERC and post-pellet IRC confinement scenarios, initial estimations of D and V profiles have been carried out using the impurity transport calculation code STRAHL [41] in order to achieve a reasonable match of measured and modeled n_{Ar}^{16+} density profiles. STRAHL solves the continuum equation radially in one dimension for all charge states of selected impurities, providing the time dependent evolution of 1D impurity emission profiles with the additional option to include impurity transport using a linear ansatz of diffusive D and convective velocity V impurity transport parameter profiles [41]. While the diffusivity profile is only positive,

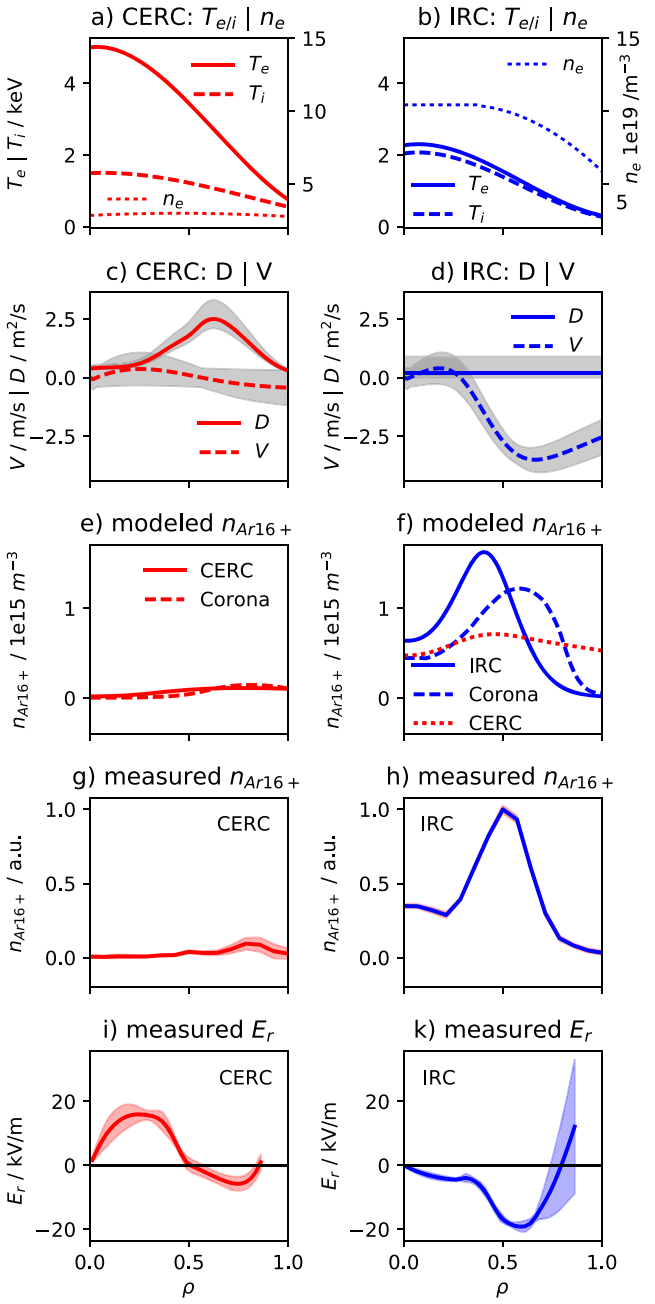

Figure 2. STRAHL modeled (*e*) and (*f*) versus experimentally obtained (*g*) and (*h*) impurity density profiles of Ar^{16+} for experimental temperature and density profiles (*a*) and (*b*) and assumed diffusive D and convective V transport parameter profiles for (*c*) high anomalous, CERC-like transport (left column) and (*d*) reduced IRC-like transport (right column) of impurities. The kinetic profiles shown in (*a*) and (*b*) are taken at times $t = 1.25$ s and $t = 1.85$ s for the CERC and IRC phases, respectively.

V can adopt positive as well as negative values, corresponding to outwards (positive V) and inwards directed (negative V) impurity pinch velocities. To perform the simulations, T_e, T_i, and n_e profiles have been used as input parameters for STRAHL and set similar to experimental profiles in the CERC and IRC phase of program 201 712 07.006 (figures 2(*a*) and (*b*)). For the CERC scenario, typical D and V profiles [32] have been used for the STRAHL calculations (figure 2(*c*)). In particular, a high anomalous, non-neoclassical diffusivity up to $D = 2.5$ m^2 s^{-1} and a neoclassical convection velocity profile has been used according to experimental findings of anomalous impurity transport in CERC plasmas of W7-X [20, 22, 32]. For the post-pellet IRC scenario, reduced anomalous transport has been observed [27, 39] and hence a reduced diffusivity is expected so that here, D has been assumed to be constant with $D = 0.2$ m^2 s^{-1} (figure 2(*d*)). As the pronounced negative E_r in the IRC is expected to attract the highly charged Ar^{16+} impurities (also reflected in the above observed negative Ar^{16+} fluxes), the convection velocity profile has been assumed accordingly with a negative value of up to $V = -4.0$ m s^{-1} (figure 2(*d*)). The resulting modeled n_{Ar}^{16+} profiles shown in figures 2(e) and (*f*) in solid lines do match the experimentally observed ones (figures 2(*g*) and (*h*)) reasonably well, both with respect to the profile shapes and also the ratio of 1/10 in the peak impurity densities comparing CERC and IRC.

To further investigate the impact of the transport parameters on the actual n_{Ar}^{16+} profile shapes, these simulations are also compared to a simple case in which transport is neglected ($v = D = 0$) and the Ar density profiles are calculated by assuming a coronal equilibrium, as shown in dashed lines in figures 2(*e*) and (*f*). As for CERC, the Ar profile is rather flat already in the Corona case, the addition of a strong D does not change the profile considerably. The situation is different in the IRC case: due to the reduced T_e profile, the Corona n_{Ar}^{16+} profile is enhanced and slightly peaked around $\rho = 0.6$, however still too broad and shifted outwards with respect to the experimental n_{Ar}^{16+} profile. Here, the assumption of the negative V profile is essential for reproducing the highly peaked experimental n_{Ar}^{16+} profile. Finally, assuming CERC transport properties with the D and V profiles of figure 2(*c*) but kinetic IRC profiles of figure 2(*b*) yields as expected a broad n_{Ar}^{16+} profile shape (dotted line in figure 2(*f*)) that does not match the experimentally observed IRC n_{Ar}^{16+} profile at all, but agrees well with the experimental CERC n_{Ar}^{16+} profile shown in figure 1(*e*), dashed line.

Compared to neoclassical expectations, the experimental D and V values in the post-pellet IRC phase are indeed reduced, but still not neoclassical. Actually, the neoclassical expected transport parameters for the IRC phase are further reduced by a factor of 10 to 5 with $D_{NC} = 0.013$ m^2 s^{-1} and $V_{NC} = -0.75$ m s^{-1} and the corresponding modeled n_{Ar}^{16+} density profile does not match the experimental one at all (not shown).

The in figures 2(*c*) and (*d*) shown D and V profile errors have been derived from an individual variation of D and V profiles, validating its effect on the modeled n_{Ar}^{16+} profiles. Note also, that the experimental n_{Ar}^{17+} profiles exhibit significant uncertainties, dominating the Γ_{Ar}^{16+} error in figure 1(*h*). Improving the n_{Ar}^{17+} profile reconstruction is currently under investigation by e.g. making use of the 2nd XICS channel [14], monitoring Ar^{17+} directly. In addition, the individual impact of the different contributions of negative E_r, reduced turbulence, and high density n_e and its profile shape to the impurity confinement cannot be disentangled from each other for the present experiment program. Here, additional experiments are required.

5. Summary and conclusions

The in this work shown experimental results of observed enhanced impurity confinement in W7-X IRC plasma scenarios, yielding one order of magnitude enhanced Ar impurity densities, peaked Ar profile shapes around the plasma mid radius and pronounced negative, inwards directed Ar fluxes, have been compared against impurity transport simulations. The experimental n_{Ar}^{16+} profile shapes could be matched by the simulations both in CERC and IRC scenarios. For the CERC phase a good match is found using D and V impurity transport profiles typical of W7-X medium density plasmas, for the post-pellet IRC phase a match can be found by assuming reduced anomalous transport ($D = 0.2$ m^2 s^{-1}) and an inward directed convection of impurities ($V = -4$ m s^{-1}). The findings for the impurity transport correlates with the improved energy confinement and reduced turbulence observed in pellet fueled IRC scenarios [27, 39].

The enhanced confinement of impurities in post-pellet IRC and in particular, the negative impurity fluxes attracting impurities into the bulk plasma, suggests that impurity accumulation may become an issue if steady-state turbulence reduced IRC scenarios become accessible on W7-X (for example with advanced density profile control). Here, future experiments are needed to verify the long term behavior of impurity transport in high-performance pellet fueled W7-X plasmas and to explore possibilities of impurity control.

Acknowledgments

This work has been carried out within the framework of the EUROfusion Consortium and has received funding from the Euratom research and training programme 2014–2018 and 2019–2020 under Grant Agreement No. 633053. The views and opinions expressed herein do not necessarily reflect those of the European Commission.

ORCID iDs

A. Langenberg https://orcid.org/0000-0002-2107-5488
Th. Wegner https://orcid.org/0000-0003-0136-0406
O. Marchuk https://orcid.org/0000-0001-6272-2605
J.M. García-Regaña https://orcid.org/0000-0001-7632-3357
N.A. Pablant https://orcid.org/0000-0001-6617-8459
S. Bozhenkov https://orcid.org/0000-0003-4289-3532

K.-J. Brunner https://orcid.org/0000-0002-0974-0457
M. Beurskens https://orcid.org/0000-0002-3354-0279
R.C. Wolf https://orcid.org/0000-0002-2606-5289

References

[1] Carralero D. *et al* 2020 *Nucl. Fusion* **60** 106019
[2] Pablant N.A. *et al* 2018 *Phys. Plasmas* **25** 022508
[3] García-Regaña J.M. *et al* 2018 *Plasma Phys. Control. Fusion* **60** 104002
[4] Buller S., Smith H., Mollén A., Newton S. and Pusztai I. 2019 *Nucl. Fusion* **59** 066028
[5] Mollén A., Landreman M., Smith H.M., García-Regaña J.M. and Nunami M. 2018 *Plasma Phys. Control. Fusion* **60** 084001
[6] García-Regaña J.M. *et al* 2017 *Nucl. Fusion* **57** 056004
[7] Helander P., Newton S.L., Mollén A. and Smith H.M. 2017 *Phys. Rev. Lett.* **118** 155002
[8] Buller S., Smith H.M., Helander P., Mollen A., Newton S.L. and Pusztai I. 2018 *J. Plasma Phys.* **84** 905840409
[9] Calvo I., Parra F.I., Velasco J.L., Alonso J.A. and García-Regaña J. 2018 *Nucl. Fusion* **58** 124005
[10] García-Regaña J.M. *et al* 2021 *J. Plasma Phys.* **87** 855870103
[11] Dinklage A. *et al* 2019 *Nucl. Fusion* **59** 076010
[12] Burhenn R. *et al* 2009 *Nucl. Fusion* **49** 065005
[13] Ford O.P. *et al* 2020 *Rev. Sci. Instrum.* **91** 023507
[14] Langenberg A. *et al* 2018 *Rev. Sci. Instrum.* **89** 10G101
[15] Wegner T. *et al* 2018 *Rev. Sci. Instrum.* **89** 073505
[16] Zhang D. *et al* 2019 *Phys. Rev. Lett.* **123** 025002
[17] Kubkowska M. *et al* 2018 *Rev. Sci. Instrum.* **89** 10F111
[18] Buttenschön B. *et al* 2016 *43rd EPS Conf. ECA* p 4.012 (https://pure.mpg.de/rest/items/item_2353913_3/component/file_3319064/content)
[19] Yokoyama M. *et al* 2007 *Nucl. Fusion* **47** 1213
[20] Langenberg A. *et al* 2020 *Phys. Plasmas* **27** 052510
[21] Langenberg A. *et al* 2019 *Plasma Phys. Control. Fusion* **61** 014030
[22] Geiger B. *et al* 2019 *Nucl. Fusion* **59** 046009
[23] Wegner T. *et al* 2020 *Nucl. Fusion* **60** 124004
[24] Xanthopoulos P. *et al* 2020 *Phys. Rev. Lett.* **125** 075001
[25] Helander P. and Zocco A. 2018 *Plasma Phys. Control. Fusion* **60** 084006
[26] Pablant N. *et al* 2020 *Nucl. Fusion* **60** 036021
[27] Bozhenkov S.A. *et al* 2020 *Nucl. Fusion* **60** 066011
[28] Baldzuhn J. *et al* 2019 *Plasma Phys. Control. Fusion* **61** 095012
[29] Wolf R.C. *et al* 2019 *Phys. Plasmas* **26** 082504
[30] Mattioli M., Giannella R., Myrnas R., Demichelis C., Denne-Hinnov B., Wit T.D.D. and Magyar G. 1995 *Nucl. Fusion* **35** 1115
[31] Svensson J. and Werner A. 2007 *Int. Symp. Intelligent Signal Processing-WISP* (3-5 October 2007) (Alcala de Henares, Spain) pp 955–60 (https://ieeexplore.ieee.org/stamp/stamp.jsp?tp= & arnumber=4447579)
[32] Langenberg A. *et al* 2017 *Nucl. Fusion* **57** 086013
[33] Langenberg A. *et al* 2019 *Rev. Sci. Instrum.* **90** 063505
[34] Rice J. *et al* 2015 *Nucl. Fusion* **55** 033014
[35] Burhenn R. *et al* 2004 *Fusion Sci. Technol.* **46** 115
[36] Kubkowska M. *et al* 2020 *J. Instrum.* **15** C01019
[37] Summers H.P. and O'Mullane M.G. 2011 *AIP Conf. Proc.* **1344** 179
[38] Brunner K. *et al* 2018 *J. Instrum.* **13** P09002
[39] Baldzuhn J. *et al* 2020 *Plasma Phys. Control. Fusion* **62** 055012
[40] Fuchert G. *et al* 2020 *Nucl. Fusion* **60** 036020
[41] Dux R. 2006 STRAHL user manual *Max-Planck-Institue for Plasmaphysics IPP Report 10/30*